scientific reports

Check for updates

OPEN

Reconfigurable on-chip optical wireless switches on SiN-TFLN hybrid platform

Muhammad Khalid[1]✉, Massimo Simone[1], Simone Ferraresi[2], Gaetano Bellanca[2], Vincenzo Petruzzelli[1] & Giovanna Calò[1]

Integrated optical phased arrays (OPAs) are becoming substantially important in modern integrated photonics because of their fast, precise and non-mechanical beam steering capabilities. In this work, we present a new approach for on-chip communication using a broadband $1 \times N$ integrated wireless switch, considering a silicon nitride-thin film lithium niobate (SiN-TFLN) hybrid platform. The proposed optical switch is based on OPAs and can address one of the in-plane receivers by properly adjusting the phase shift between the antenna elements comprising the OPA. The precise manufacturing of lithium niobate (LN) components is challenging, due to the nature of complex fabrication processes. The proposed hybrid design circumvents the challenges related to the direct etching of LN components while simultaneously exploiting the advantages of LN. We numerically demonstrate that the optical switch in the hybrid configuration exhibits improved performance as compared to the SiN-only configuration. The phase shifts required for beam steering are achieved using electro-optic effect. We also present the design of a SiN-TFLN electro-optic phase shifter and evaluate the overall energy required to drive the optical switch. We find that the phase shifter demonstrates the half-wave voltage-length product of 4.74 V cm, requiring 5.93 pJ of energy to achieve a π phase shift with an interaction region of length less than 1 cm. Moreover, we show that the total energy required by the switch to direct optical signals from transmitter to one of the receivers is 10.52 pJ. Our results demonstrate that this hybrid approach can facilitate the design and realization of integrated photonic devices with enhanced performance.

Keywords Optical phased arrays, Electro-optic phase shifters, On-chip optical communication, LNOI technology

Since the introduction of thin-film lithium niobate (TFLN) technology, there has been an increasing interest in the design and fabrication of lithium niobate integrated photonic components. Lithium niobate ($LiNbO_3$ or LN), in fact, exhibits interesting physical properties such as high electro-optic coefficients[1], strong second-order nonlinearities[2], low material losses and large transparency window[3]. TFLN platform allows exploiting the remarkable characteristics of LN and holds a strong potential for the realization of high-speed and low-loss integrated photonic devices with reduced footprints[4–7]. Despite its numerous advantages, the development of the LN integrated photonics has been slowed down due to the fact that the precise manufacturing of LN components poses several technical challenges, because of the complex etching processes involved. These fabrication-related issues of TFLN such as etching depth, rough and slanted side walls, and lithium contamination in CMOS processing limit its scalability and CMOS compatibility.

To avoid the direct etching, various hybrid integrations of LN with various materials such as silicon (Si)[8,9], silicon carbide (SiC)[10], silicon nitride (Si_3N_4 or SiN)[11–13], tantalum pentoxide (Ta_2O_5)[14] or chalcogenide glass (ChG)[15] have been considered. Among these hybrid integrations, silicon nitride is considered as a favorable material as it exhibits extremely low propagation losses, CMOS-compatible etching and high tolerance to fabrication errors[16]. SiN is widely adopted as a CMOS-grade low-loss waveguide platform. As compared to high-index (i.e., Si or LN) platform, SiN provides higher tolerance to fabrication imperfections due to its lower refractive index. This makes performance of SiN waveguides less sensitive to fabrication-related dimensional variations, and thus provides better yield. SiN is preferred over other material platforms also because it offers a broader transparency window and absence of two-photon absorption, which is advantageous for high power and low-loss CMOS photonic devices[17]. Liu et al. demonstrated a wafer-scale manufacturing process that produces

[1]Department of Electrical and Information Engineering, Polytechnic University of Bari, 70126 Bari, Italy. [2]Department of Engineering, University of Ferrara, 44122 Ferrara, Italy. ✉email: muhammad.khalid@poliba.it

ultra-low loss and high yield SiN photonic integrated devices[18]. Wafer-level bonding technology for hybrid SiN-TFLN technology has been very recently demonstrated in Ref.[19]. It is well-known that standalone SiN (SiN-only) lacks electro-optic effect and has relatively weaker nonlinearities. This hinders the realization of nonlinear and active photonic components utilizing all SiN. However, considering a hybrid approach, that is the integration of SiN on TFLN, can allow combining the advantages of both materials, while simultaneously overcoming their limitations.

Optical switches are key components in integrated photonic devices for processing and routing data. They have a broad range of applications including photonic computing, data centers and optical communication[20–22]. Conventional microring resonator (MRR)-based optical switches have limited bandwidth due to their resonant behavior, while the Mach-Zehnder interferometer (MZI)-based optical switches have high insertion losses and crosstalk[23,24]. Optical switches based on reconfigurable optical phased arrays (OPAs) are particularly attractive due to their ability to dynamically control and steer optical signals through phase control rather than mechanical movement, and due to their low power consumption. Optical switching technology for data centers is also attracting significant interest. This is because bandwidth constraints and high power consumption in traditional electrical and wire-based switches pose challenges for data centers. Data centers require advanced solutions to manage their exponentially growing traffic and to address these limitations. Optical networks promise faster data transfer, reduced power consumption and low latency within data centers. Within optical networks, these wireless switches can facilitate broadband reconfigurable on-chip communication. They can be used to transmit WDM signals allowing parallel transmission of various data channels, and to enhance connectivity within different processing units in densely integrated computing architectures[25,26]. In an MRR-based network, to switch a WDM signal over the network, multiple MRRs must be cascaded and an increase in the WDM channels leads to an impairment of the overall power budget due to the high number of MRRs required[27]. Optical wireless switches have several advantages over wire-based optical switches. For example, they are more energy efficient, reliable and enable improved scalability. Wireless switches also offer greater reconfigurability and flexibility by reducing the need for physical connections. OPAs are considered as a promising technology for the next-generation integrated photonic devices as they enable high-speed and precise beam steering and beam shaping non-mechanically[28]. Reconfigurable OPAs are being actively researched in a variety of different potential applications, such as low-cost LiDAR[29], space optical communication[30], lens-less imaging[31], augmented reality and biophotonics[32]. OPA-based optical wireless switches for on-chip communication considering silicon-on-insulator and TFLN technologies have been numerically investigated in[25,26,33,34]. It has been demonstrated that the performance of these optical switches is strongly influenced by the link distance, owing to the multipath effects originating from multiple reflections from the material discontinuities of the typical multilayer configuration in integrated photonics. Very recently, optical phased arrays implemented in the SiN platform have been proposed for two-dimensional out-of-plane beam steering using SiN grating antennas[13]. Silicon nitride OPAs can be fabricated using CMOS-compatible processes and offer lower power consumption, which make them suitable for on-chip integration. However, phase shift in SiN OPAs is generally driven by the thermo-optic effect due to lack of electro-optic effect in SiN[35]. These thermo-optic phase shifters are less suitable for reconfigurable OPAs as they have high power consumption and low beam-steering speed. To cope with the limitations of the thermo-optic phase shifters, electro-optic phase shifters based on the hybrid SiN-TFLN have been considered in[13], since lithium niobate exhibits a large electro-optic coefficient, high modulation speed and low power consumption.

In this work, we present a $1 \times N$ reconfigurable optical switch based on OPAs implemented in hybrid SiN-TFLN platform for on-chip communication. In this switch, a transmitter can direct an optical signal to one of the N in-plane receivers. To the best of our knowledge, the on-chip wireless propagation in SiN-TFLN technology has never been studied before. The novelty of the proposed device lies in integrating LN with SiN for vertical field confinement, while retaining the in-plane beam steering capability of the OPAs. The advantages of introducing the LN layer are twofold. First, it provides vertical field confinement due to a high refractive index contrast with the cladding medium, which can lead to improved performance of the optical wireless switch by reducing radiation leakage into the cladding material. Second, it can reduce the multipath propagation effects originating from multiple reflections from material discontinuities in a typical multi-layer configuration in integrated photonics. In particular, we present an example of 1×3 optical switch in which the OPAs at the transmitter and at each receiver are composed of three identical SiN taper antennas. The phase shift between the antenna elements of the OPA is driven through the electro-optic phase shifters. Numerical simulations have been performed based on three-dimensional finite-difference-time-domain (FDTD) method[36]. To highlight the advantages of the hybrid SiN-TFLN implementation, we first present an analysis of the optical wireless switch based on OPAs composed only of SiN antennas immersed in silica (without introducing the TFLN). Then, we evaluate the performance of the switch in hybrid SiN-TFLN material configuration. We demonstrate that the implementation of the switch in hybrid SiN-TFLN leads to an improved performance as compared to the SiN-only optical switch. This is because the optical field is vertically confined mostly within the thin layer of LN and the multipath propagation effects in this case become less critical. Moreover, we also present the design of SiN-TFLN electro-optic phase shifters needed to drive the optical switch and evaluate the overall energy required for beam steering.

OPA-based optical switch

The schematic illustration of a 1×3 optical switch based on reconfigurable OPAs is presented in Fig. 1a, in which a transmitter can direct an input signal to one of the three in-plane receivers at the output. The typical multilayer configuration of SiN-TFLN samples has been considered in the simulations, as depicted in Fig. 1b. The multilayer consists of a bottom silicon (Si) layer supporting a 3 μm thick oxide layer (SiO_2). Atop a thin layer of lithium niobate with a thickness t_{LN} is deposited on which SiN taper antennas are etched. The width and thickness of the SiN waveguides are W_{SiN} and t_{SiN}, respectively. The center-to-center distance between two

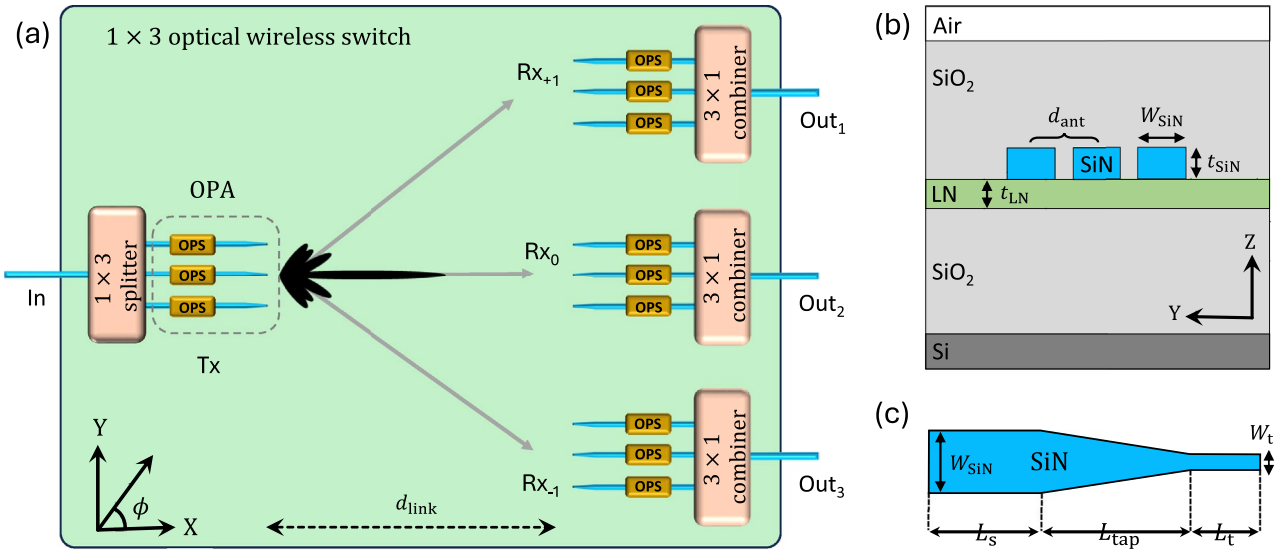

Fig. 1. (**a**) Schematic illustration of the 1×3 optical switch in which a transmitter Tx can address three in-plane receivers. (**b**) Cross-section view at the input of the optical switch. The phase shift between the antenna elements of the OPAs is driven by the optical phase shifters (OPS) to address one of the three in-plane receivers. (**c**) Geometry of the SiN taper antenna serving as a basic building block in OPAs.

adjacent antennas is d_{ant}. The structure is covered with a finite (3 μm thick) SiO_2 cladding layer, interfaced with air.

As depicted in Fig. 1a, the transmitter Tx is composed of a multimode interference (MMI) power splitter, optical phase shifters (OPS) and an optical phase array (OPA). Similarly, each receiving node Rx_i $(i = 0, \pm 1)$ is made of an OPA, OPS and an MMI combiner. We envision that in this design, all components including MMI splitter/combiner, optical phase shifters and optical phased arrays are integrated on the same photonic chip. The design and operation principles of $1 \times N$ power splitter and $1 \times N$ power combiner (N being the number of output/input ports) have been recently reported considering TFLN technology[37]. The MMI splitters/combiners are implemented in the same layer as the optical phase shifters and optical phased arrays. Each OPA at the transmitter and the receivers is made of three identical SiN taper antennas. The geometry of the taper antenna forming the OPAs is shown in Fig. 1c. It consists of an input straight waveguide of width W_{SiN} and length L_{s}, an inversely tapered waveguide of length L_{tap}, and a taper tip made of a narrow straight waveguide of width W_{t} and length L_{t}. The thickness t_{SiN} of the SiN waveguide remains constant throughout the structure. We study the fundamental transverse-electric mode of the structure in the 2D cross-section (in the YZ-plane) to extract the effective indices at the free-space wavelength $\lambda = 1550$ nm. The extracted effective indices are then used to design the taper antenna, which serves as the fundamental element in the OPAs. For an efficient radiation, the taper must convert the propagating mode at the input waveguide into an evanescent mode at the taper tip. Therefore, for the input part of the taper antenna (input straight waveguide), we choose geometrical dimensions to exhibit a well-confined propagating mode. The dimensions of the narrow straight waveguide forming the tip of the taper corresponds to the evanescent mode. Throughout this work, we consider $W_{\mathrm{t}} = 150$ nm, $L_{\mathrm{s}} = L_{\mathrm{t}} = 1$ μm and $L_{\mathrm{tap}} = 2$ μm, as used for the taper antennas in[34].

The phase shift in each taper antenna is governed by the OPS, and depending upon the phase shift between the unit radiators of the OPAs, the input signal can be steered to address one of the three in-plane receivers Rx_i $(i = 0, \pm 1)$. The transmitter Tx and the broadside receiver (Rx_0) are separated by a link distance d_{link}, and the center-to-center distance between the in-plane receivers is Δy. We numerically analyze the performance of the on-chip optical switch in terms of insertion loss $\mathrm{IL} = -10\log(\mathrm{T}_i)$ and crosstalk $\mathrm{XT}_{i,j} = 10\log(\mathrm{T}_j) - 10\log(\mathrm{T}_i)$, where T_i and T_j respectively represents the transmittance (i.e., the ratio between the received and the transmitted powers) at the addressed receiver Rx_i $(i = 0, \pm 1)$ and the non-addressed receiver Rx_j $(j = 0, \pm 1)$, with $i \neq j$. Both the wavelength dispersion and the material anisotropy of LN have been taken into account in our numerical simulations, which are based on the 3D-FDTD method[36]. LN has an anisotropic refractive index, which can be expressed in the matrix form as:

$$n_{\mathrm{LN}} = \begin{pmatrix} n_{\mathrm{o}} & 0 & 0 \\ 0 & n_{\mathrm{e}} & 0 \\ 0 & 0 & n_{\mathrm{o}} \end{pmatrix} \tag{1}$$

where n_{o} and n_{e} represent the ordinary and extra-ordinary refractive indices. At the operating wavelength $\lambda = 1550$ nm, the ordinary and extra-ordinary refractive indices of LN are $n_{\mathrm{o}} = 2.21$ and $n_{\mathrm{e}} = 2.14$, respectively, whereas the refractive index of SiN is $n_{\mathrm{SiN}} = 1.99$[12]. We consider an X-cut LN crystal with optic axis aligned with the Y-axis of the Cartesian coordinate system. In the context of hybrid SiN-TFLN platform, the

impact of anisotropy of the LN on the mode confinement and electro-optic tuning is discussed in a very recent work[38].

Optical switch in SiN-only configuration

The on-chip wireless communication is strongly dependent on the multilayer configuration in which the optical signal is radiated, as numerically and experimentally demonstrated in[33,34,39]. In order to better evaluate the effect of introducing a thin film of lithium niobate in the multilayer stack, we first consider a simpler configuration for the 1×3 on-chip optical wireless switch in which we assume that the OPAs are made only of SiN waveguides embedded in SiO_2, without introducing the TFLN layer. The input cross-section of this SiN-only configuration is shown in Fig. 2a, whereas the switch configuration is equal to the one shown in Fig. 1a.

We consider that each OPA at the transmitter and the receivers is constructed from $\mathrm{N_{ant}} = 3$ identical SiN taper antennas, $\mathrm{N_{ant}}$ being the number of antennas forming the OPAs. The input SiN waveguides have a width $W_{\mathrm{SiN}} = 600$ nm and a thickness $t_{\mathrm{SiN}} = 300$ nm which are chosen to guarantee the propagation of a single (fundamental TE) mode. Moreover, we consider that the adjacent antenna elements of OPAs are separated by a center-to-center distance $d_{\mathrm{ant}} = W_{\mathrm{SiN}} + \lambda_m/4$, where $\lambda_m = \lambda/n_{\mathrm{SiO_2}}$ with $\lambda = 1550$ nm being the input wavelength and $n_{\mathrm{SiO_2}} = 1.445$ is the refractive index of the silica cladding. The separation between the receivers is determined by the relation $\Delta y = d_{\mathrm{link}} \tan(\Phi)$ where $\Phi = \pm \sin^{-1}(\lambda_m/(d_{\mathrm{ant}}\mathrm{N_{ant}}))$, which approximates the angular position of the radiation minima in the radiation pattern of the OPA[25].

It is essential to remark that this multilayer configuration suffers from the multipath propagation effects originating from the material discontinuities present in on-chip optical communication scenarios[33,34,39]. The multiple reflections occurring at the multiple interfaces give rise to constructive and destructive interference along the propagation direction, and therefore can increase or decrease the received power at an addressed receiver. Experimental demonstrations of these multipath propagation effects have been reported in the literature[39,40]. In these works, non-reconfigurable wireless links were fabricated and characterized using SOI technology, showing a very good agreement between the measurements and the FDTD simulations.

As depicted in Fig. 2, the transmitter can establish a communication with one of the three receivers, provided that a suitable phase shift is applied at the input of the antenna elements of the OPA. Let α denote the phase shift between the radiating antennas of the OPAs. When the phase difference between antenna elements is zero, i.e., $\alpha = 0°$, the transmitter communicates with the central receiver $\mathrm{Rx_0}$. The beam steering to address the

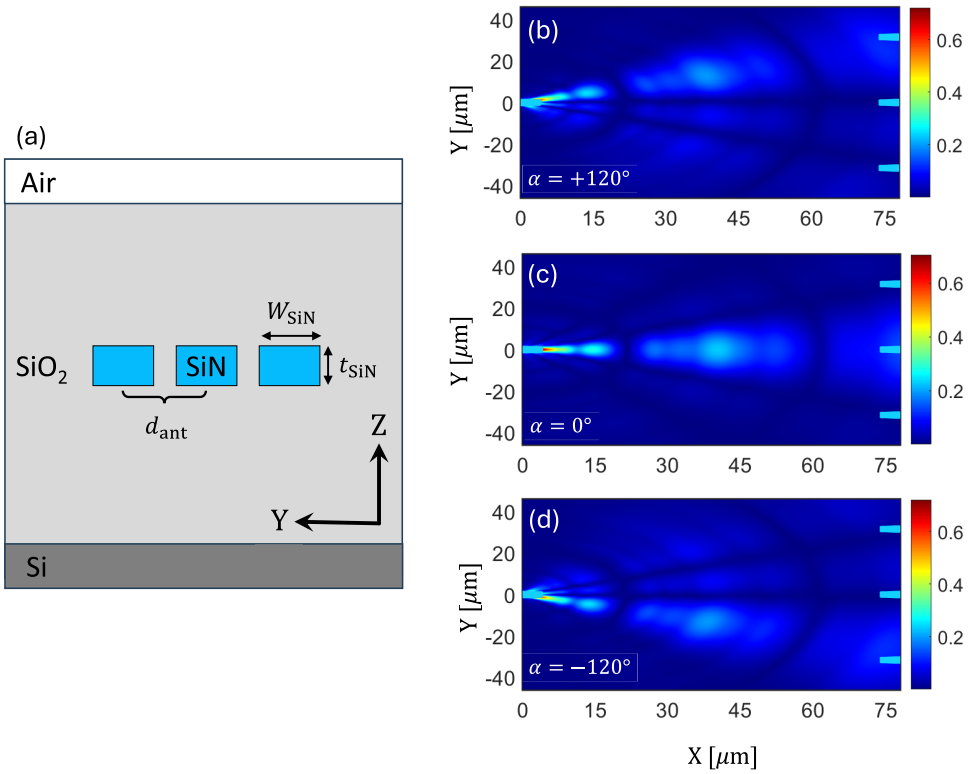

Fig. 2. (**a**) Cross-section view at the input of the SiN optical wireless switch. The SiN taper antennas forming the OPAs are embedded in SiO_2 with the refractive index $n_{\mathrm{SiO_2}} = 1.445$. This structure is based on a multilayer configuration with a lower silicon (Si) layer and an upper air layer. Electric field $|E|$ profile in the XY-plane (at Z = 0), when the transmitter aims: (**b**) at the upper receiver with phase shift $\alpha = +120°$ between the antenna elements; (**c**) at the broadside receiver with $\alpha = 0°$, and (**d**) at the lower receiver with $\alpha = -120°$, demonstrating the in-plane beam steering. The field are plotted at the operating wavelength $\lambda = 1550$ nm for an arbitrarily chosen link distance $d_{\mathrm{link}} = 70$ µm.

upper Rx_{+1} or the lower Rx_{-1} receiver can be achieved by applying a phase shift $\alpha = \pm 360^\circ/\mathrm{N_{ant}} = \pm 120^\circ$ between the antenna elements. The electric field $|E|$ distribution as shown in Fig. 2 is calculated using 3D-FDTD simulations in the XY-plane (azimuthal plane), for an arbitrarily chosen link distance $d_{\mathrm{link}} = 70\ \mu$m and at the operating wavelength $\lambda = 1550$ nm. The field maps demonstrating a connection between the upper, central and lower receiver for the input phase shift $\alpha = +120^\circ$, $\alpha = 0^\circ$ and $\alpha = -120^\circ$, are shown in Fig. 2b–d, respectively. The results show that the electric field exhibits constructive and destructive interference patterns originating from the multiple reflections at the lower Si and upper air layers. The field maxima and minima can be observed along the propagation direction.

Figure 3 shows the transmittance computed at each receiver as a function of the link distance d_{link}. Modifying the link distance means shifting the receivers toward or away from the transmitter, which can place them at the interference maxima or minima. Specifically, Fig. 3a–c show, respectively, the transmittance at each receiver when the transmitter points at the lower receiver Rx_{-1} ($\alpha = -120^\circ$), at the broadside receiver Rx_0 ($\alpha = 0^\circ$), and at the upper receiver Rx_{+1} ($\alpha = +120^\circ$). It can be noticed that in each case the addressed receiver gets a maximum radiated power whereas the non-addressed receivers receive minimum signal. The oscillations in the transmittance correspond to the constructive and destructive interference induced by multiple reflections. These results suggest that the addressed receiver can get a higher or lower received power depending upon the link distance between the transmitter and the receiver, and therefore, it becomes crucial to carefully position the receivers to get an optimal power. It is also important to point out that, for an optimal reception of the transmitted power, a suitable phase shift ($-\alpha$) is also required at the receiving OPA to virtually align its beam in the direction of maximum radiation, i.e., towards the transmitting OPA[25].

Optical switch in hybrid SiN-TFLN configuration

Now, we evaluate the performance of the hybrid SiN-TFLN 1×3 optical switch, with structure configuration schematized in Fig. 1. In this case, it is considered that the SiN waveguides comprising the OPAs are etched on a thin layer of LN of thickness $t_{\mathrm{LN}} = 400$ nm. The simulation setup and the geometrical parameters for SiN waveguides are exactly the same as described in the previous section, with an exception of introducing the thin layer of LN.

The transmittance T at each receiver as function of operating wavelength λ for different values of the phase shift parameter α is plotted in Fig. 4a–c, considering the link distance $d_{\mathrm{link}} = 70\ \mu$m. The dotted-dashed lines in Fig. 4a–c represent the transmittance in the SiN-only setup, and are reported for comparison. It can be observed that in both configurations, the optical switch shows a broadband behavior in the entire C-band, but the SiN-TFLN exhibits a lower insertion loss. This broadband behavior can allow the implementation of wavelength division multiplexing (WDM) communication schemes to transmit simultaneously various wavelength channels. For the SiN-TFLN configuration, the insertion loss change is less than 0.2 dB over the considered wavelength range both for the broadside ($\alpha = 0^\circ$) and the off-axis ($\alpha = \pm 120^\circ$) communication. It is important to note that in this case the received power is higher (~3.5 dB higher for $\alpha = 0^\circ$ and ~4.4 dB higher for $\alpha = \pm 120^\circ$, at $\lambda = 1550$ nm and $d_{\mathrm{link}} = 70$ μm) as compared with the one received in SiN-only case.

Figure 4d–f show the electric field $|E|$ profile in the XY-plane at Z=0 (i.e., in the middle of LN layer), demonstrating the link connection with the upper receiver ($\alpha = +120^\circ$), the broadside receiver ($\alpha = 0^\circ$) and the lower receiver ($\alpha = -120^\circ$). The field maps are plotted at the operating wavelength $\lambda = 1550$ nm considering a link distance $d_{\mathrm{link}} = 70$ μm. Notably, when the transmitter addresses a particular receiver the other non-addressed receivers fall at radiation minima. It is important to note that the map plots in Fig. 4d–f do not show

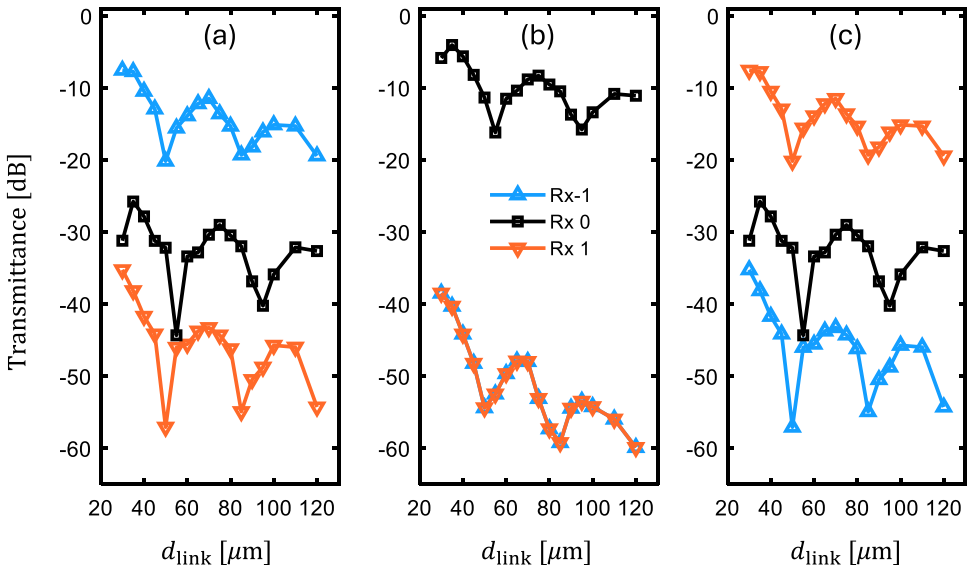

Fig. 3. Transmittance at each receiving node as a function of link distance d_{link}, calculated at $\lambda = 1550$ nm. The phase shift between the antenna elements is (**a**) $\alpha = -120^\circ$, (**b**) $\alpha = 0^\circ$ and (**c**) $\alpha = +120^\circ$.

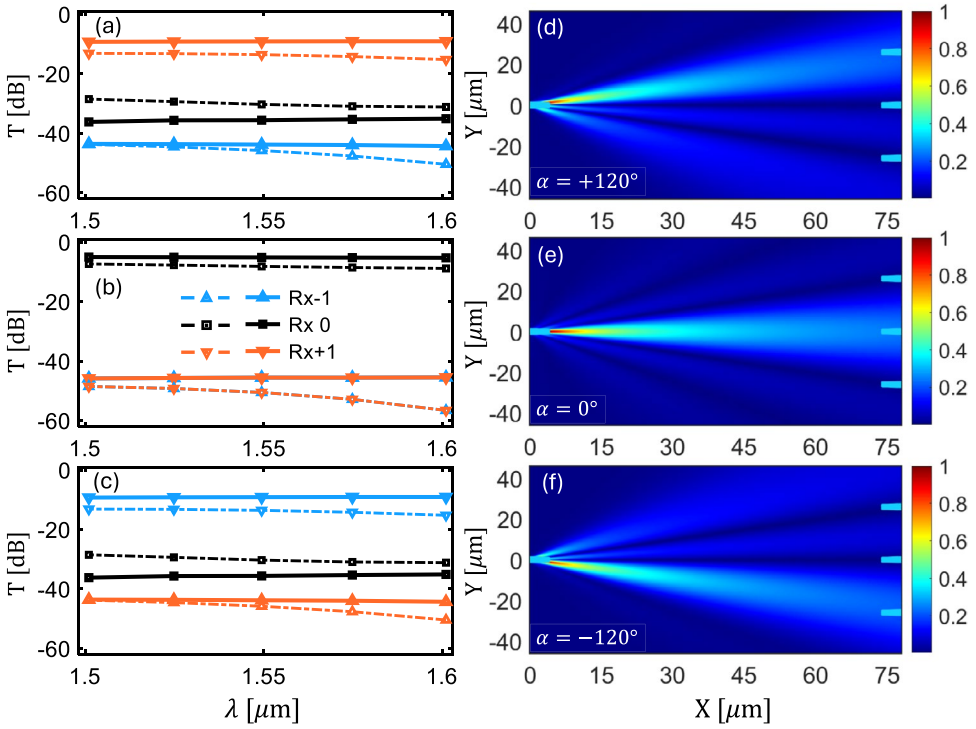

Fig. 4. Transmittance T at each receiver as a function of operating wavelength λ, calculated using 3D-FDTD simulations for a link distance $d_{\text{link}} = 70$ μm. The results are plotted for different values of the phase shifts between the radiating antennas: (**a**) $\alpha = +120°$, (**b**) $\alpha = 0°$ and (**c**) $\alpha = -120°$. The dotted-dashed lines represent the transmittance in the SiN-only setup, and are reported for comparison. The electric field $|E|$ profiles in the XY-plane, calculated in the middle of the LN layer, demonstrating the beam steering are plotted in (**d–f**), respectively, at the operating wavelength $\lambda = 1550$ nm.

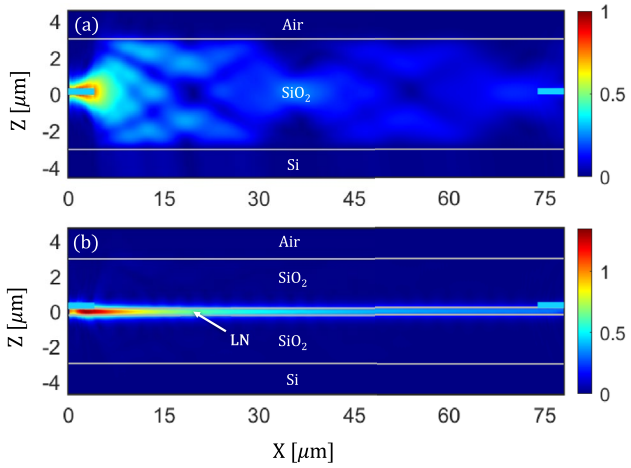

Fig. 5. Electric field $|E|$ distribution of the optical link in the XZ-plane at Y = 0, considering (**a**) the SiN-only configuration, and (**b**) the SiN-TFLN hybrid configuration. The map plots are calculated for the broadside connection at the operating wavelength $\lambda = 1550$ and a link distance of $d_{\text{link}} = 70$ μm.

any interference signature. This is in contrast to the previous case (SiN-only configuration), in which it becomes crucial to appropriately choose the link distance for the addressed receiver to get a maximum received power. In fact, in the hybrid SiN-TFLN implementation, the multipath propagation effects are less critical, as the mode is vertically more confined within the LN layer. This difference can be seen more clearly in Fig. 5, which shows a comparison between the electric field distribution in the SiN-only configuration (Fig. 5a) and in the SiN-TFLN configuration (Fig. 5b). The electric field $|E|$ profiles are calculated in the XZ-plane at Y=0, assuming that the transmitter is communicating with the broadside receiver ($\alpha = 0°$).

The results show that in the SiN-only configuration the field is radiated in the silica region exhibiting interference patterns arising from the multiple reflections at the bottom Si and upper air layers. Conversely, in the hybrid SiN-TFLN setup the field is vertically confined mostly in the LN layer, thus preventing the multipath propagation effects.

This is important to highlight that in both SiN-only and hybrid SiN-TFLN configurations, the input mode is the fundamental TE mode. In the SiN-only case, the optical field is radiated in the surrounding silica region as it propagates. This behavior, illustrated in Fig. 5a, indicates that in the SiN-only configuration, the field is confined in the silica region. In contrast, in the SiN-TFLN setup, the optical field is primarily guided within the LN thin layer, resulting in a stronger vertical field confinement compared to SiN-only platform. This can be observed in Fig. 5b where the optical field remains localized within the TFLN region rather than radiating into the silica. It is also worth mentioning that vertically confining the electromagnetic field in the thin LN layer suppresses the multipath propagation effect, which gives rise to the oscillations of the field intensity along the propagation direction (as shown in Fig. 2b–d). Conversely, this vertical confinement in the LN layer does not necessarily reduce the crosstalk between the receivers. Multipath propagation effect and crosstalk can be regarded as different phenomena. Multipath propagation effect refers to the phenomenon originating from multiple reflections from the material discontinuities of the typical multilayer configuration in integrated photonic circuits. The reflected signals undergo constructive and destructive inference along the propagation path which can significantly impact the amount of power received by the receivers. The crosstalk, in the present scenario, refers to the unwanted coupling between the nearby receivers. For example, power intended for an addressed receiver leaks into the neighboring receivers. This phenomenon is mainly related to the radiation characteristics of the OPA, such as the null and the side lobe positions. Introducing the thin layer of LN prevents the multipath propagation effect but the crosstalk between the adjacent receivers is still present although it is lower in some cases (see Fig. 6).

The transmittance at Rx_{-1} ($\alpha = -120^\circ$), Rx_0 ($\alpha = 0^\circ$), and Rx_{+1} ($\alpha = +120^\circ$) evaluated as a function of the link distance d_{link} at $\lambda = 1550$ nm is plotted in Fig. 6a–c, respectively. For comparison purpose, we also report results for the SiN-only switch, represented by the dashed lines. It is worth highlighting that, when the phase shift between the antenna elements of the OPA is zero (i.e., $\alpha = 0^\circ$), the insertion loss is lower as compared to SiN-only case for all considered link distances. However, for some link distances the crosstalk $\mathrm{XT}_{\pm 1,0}$ is slightly higher when the transmitter communicates with the broadside receiver ($\alpha = 0^\circ$), but still remains below -30 dB. For the steered beam ($\alpha = \pm 120^\circ$), on the other hand, both the insertion loss and the crosstalk improve. It can be noted that the optical switch in the SiN-TFLN configuration shows an improved performance as compared to the SiN-only one. Moreover, as expected, the hybrid SiN-TFLN case exhibits no oscillations related to the interference when varying the link distance. The absence of this oscillatory behavior results from the field confinement within the LN layer. A similar effect of field confinement and reducing multipath propagation effects can also be achieved by using a SiN-ridge waveguide design. However, SiN lacks electro-optic effect and has relatively weaker nonlinearities, which hinders the realization of active and nonlinear photonic components. Furthermore, to drive reconfigurable OPAs with high-speed beam steering, phase shifters based on electro-optic effect are more suitable. In this context, using an electro-optic material such as LN is a preferred choice.

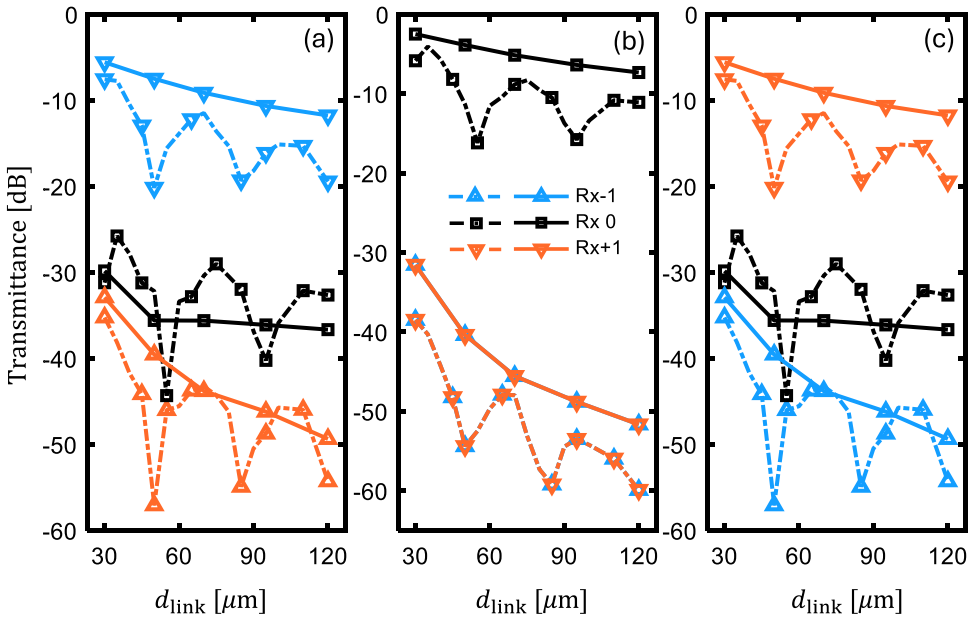

Fig. 6. Transmittance computed at each receiving node in the hybrid SiN-TFLN configuration (solid lines) and the SiN-only configuration (dashed-lines) of the 1×3 optical wireless switch. The results are plotted when the phase shift between the antenna elements is (**a**) $\alpha = -120^\circ$, (**b**) $\alpha = 0^\circ$ and (**c**) $\alpha = +120^\circ$. The dashed lines, representing the results for SiN-only configuration without any TFLN layer, are reported for comparison.

Although SiN exhibits higher tolerance to fabrication-related dimensional variations, in a hybrid platform such as SiN-TFLN, the thickness variation of the SiN waveguide and of the LN is unavoidable during the fabrication processes, which can influence device performance. For example, as recently demonstrated in Ref.[38] (See Supplementary Material of Ref.[38]), fabrication imperfection in the hybrid SiN-TFLN can alter the effective index distribution of the guided modes and can lead to the discrepancies between theoretical predictions and experimental results. Therefore, it is worth analyzing the impact of the variation of the thickness of the SiN and LN layers due to fabrication imperfection on the performance of OPA-based optical wireless switch. Figure 7 plots the transmittance calculated at each receiver as a function of thickness t_{SiN} of the SiN waveguide and as a function of thickness t_{LN} of the LN layer for different values of the phase shift angle α. The results in Fig. 7a–c show that the insertion loss is almost unaffected by the change of t_{SiN} both for the broadside and steered communication. Whereas, in the steered case, the crosstalk increases as the thickness of the SiN waveguide increases. This can be related to the change in the effective index caused by the thickness variation, which tends to broaden the main lobe and to increase the sidelobes. For the broadside communication ($\alpha = 0^{\circ}$), the behavior remains unchanged, however, for the steered communication ($\alpha = \pm 120^{\circ}$), the broadened lobe overlaps the neighboring receivers. In Fig. 7d–f, we notice that for steered communication, as the thickness t_{LN} of the LN layer increases, the crosstalk between the receivers reduces. This is because a thicker LN layer provides a better field confinement, keeping the mode well localized and therefore, reducing the crosstalk. We selected $t_{\mathrm{LN}} = 400$ nm, as this is a commonly used thickness of LN in fabricated samples[13,19].

SiN-TFLN electro-optic phase shifter

Optical phase shifters are fundamental components in reconfigurable optical phased arrays as accuracy of beam steering is strongly dependent on the phase shift applied between the antenna elements of the OPAs. In this section, we present the design of the electro-optic phase shifters in the SiN-TFLN hybrid platform, and compute the energy required to drive the phase shifters for beam steering in the OPA-based 1×3 optical switch, discussed in the previous section. The cross-section of the phase shifter is illustrated in Fig. 8a, which consists of a SiN strip waveguide on a thin layer of LN with a silica (SiO_2) cover layer. Two parallel gold (Au) electrodes (one for signal and the other for ground), each with a width $W_{\mathrm{E}} = 5$ μm and a thickness $t_{\mathrm{E}} = 0.5$ μm are placed directly over the thin layer of LN, and are separated by a gap distance g. To align with the configuration setup of the hybrid SiN-TFLN optical switch discussed earlier, we consider the same multilayer structure also for the phase shifter.

The electro-optic effect of LN is exploited to achieve the required phase shift by applying a bias voltage V_0 through the Au electrodes. The applied voltage at the electrodes modifies the refractive index of the lithium niobate, which in turn can be used to control the phase of the optical signal propagating in the waveguide. The quasi-static field distribution is calculated using finite-element-method (FEM) by using a voltage V_0 at

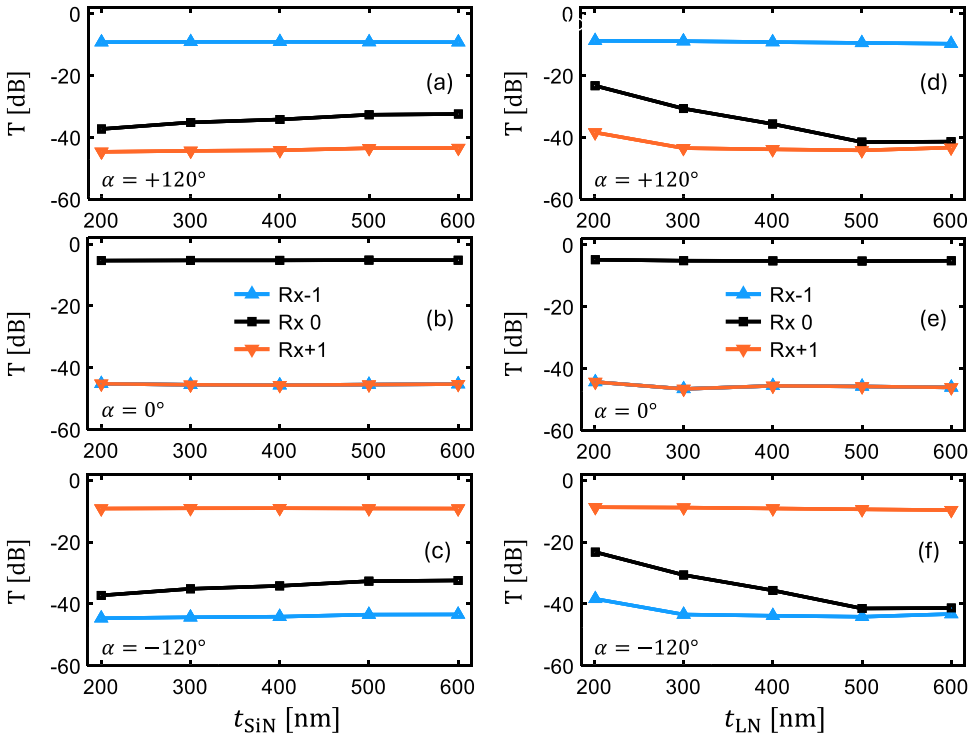

Fig. 7. Transmittance (T) computed at each receiver of the 1×3 optical wireless switch in the hybrid configuration: (**a–c**) as function of thickness of the SiN waveguide t_{SiN}, and (**d–f**) as function of thickness of the LN layer tLN. The results are computed for different values of the phase shift parameter α, as indicated on the subfigures.

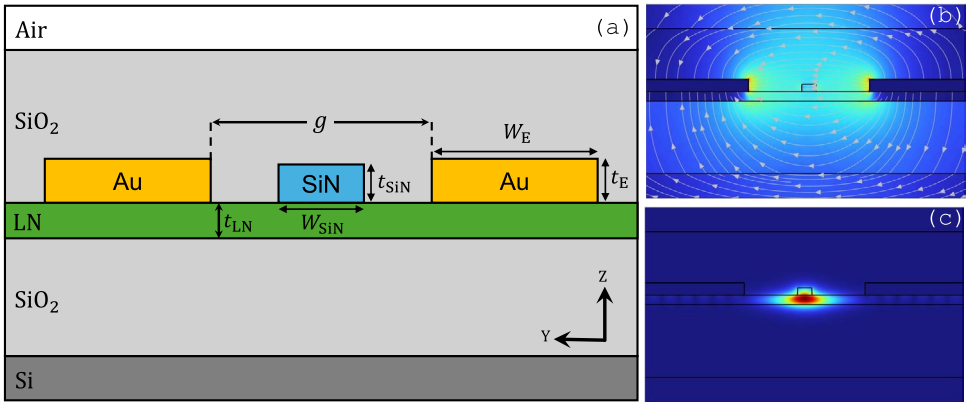

Fig. 8. (**a**) Cross-sectional schematic of the electro-optic phase shifter in hybrid SiN-TFLN configuration. The optical phase shifter is designed to drive the phase shift α between the antenna elements of the OPAs forming the 1×3 optical switch. Cross-section view of the simulated (**b**) RF electric field distribution plotted for an applied voltage V_0=1 V by considering a gap $g = 5$ μm between the gold (Au) electrodes, and (**c**) the corresponding fundamental optical TE mode at $\lambda = 1550$ nm.

the Au electrodes. Since the frequency of the applied voltage is much lower than that of the optical signal, the resulting radio frequency (RF) electric field can be considered as quasi-static field. This electric field distribution is responsible for the change of the LN refractive index, according to the following equations[41]:

$$\Delta n_{\mathrm{o}} = -\frac{1}{2} n_{\mathrm{o}}^3 r_{13} E_y \tag{2}$$

$$\Delta n_{\mathrm{e}} = -\frac{1}{2} n_{\mathrm{e}}^3 r_{33} E_y \tag{3}$$

where $r_{13} = 9.6$ pm/V and $r_{33} = 30.9$ pm/V are the electro-optic coefficients associated with the ordinary and extra-ordinary refractive indices of LN, respectively. E_y is the component of the RF electric field along the Y-direction. The electro-optic effect is maximum when the RF electric field is parallel to the optic axis of the LN material, which in the present scenario is aligned with the Y-axis of the Cartesian coordinate system. Depending on the direction of the applied electric field, an increase or a decrease in the refractive index variation can be obtained. This refractive index variation $\Delta n_{\mathrm{o,e}}$, induced by the electro-optic effect, is then taken into account in the electromagnetic analysis of the waveguide structure shown in Fig. 8a. The electro-optic effect results in a variation of the effective refractive index Δn_{eff} of the fundamental optical TE mode and can be defined as: $\Delta n_{\mathrm{eff}} = n_{\mathrm{eff}}(V_0) - n_{\mathrm{eff}}(0)$, where $n_{\mathrm{eff}}(V_0)$ is the effective refractive index at an applied voltage $V = V_0$ and $n_{\mathrm{eff}}(0)$ is the effective refractive index at $V = 0$. This effective refractive index variation Δn_{eff} can be used to determine the phase shift α by the following relation:

$$\alpha = \frac{2\pi}{\lambda} \Delta n_{\mathrm{eff}} L \tag{4}$$

where L is the length of the Au electrodes. The electrode length necessary to obtain a π phase shift is $L_\pi = \lambda/(2\Delta n_{\mathrm{eff}})$.

The simulated RF electric field distribution, when an arbitrarily chosen bias voltage $V_0 = 1$ V is applied at the Au electrodes separated by $g = 5$ μm, is depicted in Fig. 8b. The fundamental optical TE mode profile at $\lambda = 1550$ nm is plotted in Fig. 8c. It can be seen that the optical mode is reasonably well confined within the thin layer of LN under the SiN waveguide. It is worth highlighting that the presence of the metal electrodes introduces a loss contribution, which can be minimized by properly choosing the gap g. A wider separation between the electrodes can offer lower losses, but at the price of weaker electro-optic interaction (smaller effective index variation), resulting in a longer device footprint, i.e., larger $V_\pi L_\pi$ with V_π being the half-wave voltage. The $V_\pi L_\pi$ (half-wave voltage-length product) is a key parameter to assess the performance of electro-optic phase shifters. For a given V_π, the smaller index variation requires longer electrodes to achieve a π phase shift, because $L_\pi \propto 1/\Delta n_{\mathrm{eff}}$. Therefore, there exists a trade-off between the propagation loss and $V_\pi L_\pi$ product.

Figure 9a plots the half-wave voltage-length product ($V_\pi L_\pi$) and the propagation loss as a function of gap g between the electrodes. The propagation loss is plotted considering $V_\pi = 5$ V. It is observed that while the $V_\pi L_\pi$ is lower for smaller gaps, the loss increases rapidly as the gap decreases. We find that the gap value $g = 6.5$ μm provides a better trade-off between the voltage-length product and the propagation loss, as highlighted with a dashed rectangle in Fig. 9a. In particular, for $g = 6.5$ μm, we have evaluated $V_\pi L_\pi = 4.74$ V cm and 1 dB/cm propagation loss. The energy (in pico-joules) as a function of phase shift α is plotted in Fig. 9b. The energy consumption is calculated using $\mathrm{E} = CV_0^2/2$, where $C = 0.475$ pF is the numerically estimated capacitance of the electrodes. Our simulation results show that the energy required to get a π phase shift is 5.93 pJ for an applied voltage $V_\pi = 5$ V, requiring 0.95 cm long electrodes separated by a gap distance $g = 6.5$ μm. It is significant to

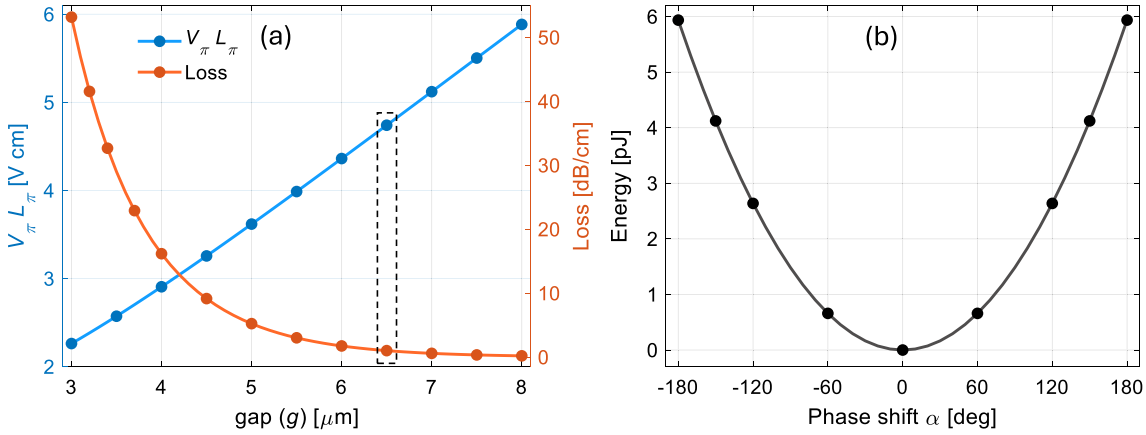

Fig. 9. (**a**) Half-wave voltage-length product ($V_\pi L_\pi$) and the propagation losses as a function of electrode gap distance g. The propagation loss is plotted considering $V_\pi = 5$ V. The dashed rectangle points out the gap value providing a better trade-off between the $V_\pi L_\pi$ and the propagation loss. (**b**) Energy in pico joules as a function of phase shift α. The energy is plotted at the trade-off gap value $g = 6.5$ μm, requiring $L_\pi = 0.95$ cm at $V_\pi = 5$ V.

Year	Phase shift (°)	Electrode gap (μm)	V_π (V)	L_π (cm)	$V_\pi L_\pi$ (V cm)	Energy (pJ/π)	Loss (dB/cm)
2023 [Ref.[16]]	180	6	22	0.4	8.8	–	0.1
2024 [Ref.[13]]	180	7	3.79	1.56	5.92	4.6	2.03 [Exp.]
2025 [Ref.[19]]	180	6.5	5.7	0.5	2.85	-	< 0.1
This work	180	6.5	3.4	0.95	4.75	5.93	0.92

Table 1. Comparison of phase shifter performance parameters. The result of present work are compared with those reported in literature[13,16,19]. V_π and L_π are the applied voltage and length of the electrodes to achieve a π phase shift, respectively. 'Exp.' refers to the experimental measured value.

emphasize that the energy consumption to achieve a π phase shift can be reduced by using a lower V_π value but at the price of longer device length. For example, using $V_\pi = 3$ V, the energy consumption can be decreased to 3.56 pJ but it will require 1.58 cm long electrodes. Our results are comparable with those reported very recently in[13] for an electro-optic phase modulator implemented in SiN-TFLN hybrid material platform. Reference[13] reports a half-wave voltage-length product $V_\pi L_\pi = 5.92$ V cm and an energy consumption of 4.6 pJ/π using 1.56 cm long electrodes with a gap distance $g = 7$ μm. It has been demonstrated that the fabricated sample presents a propagation loss of 2.03 dB/cm. A comparison between our simulation results and those recently reported in literature[13,16,19] is presented in Table 1. Note that the key performance parameters can be minimized by optimizing the geometry of the phase shifter, which is determined by the waveguide width, thickness and the spacing between the metal electrodes. In this case, however, we adopt the phase shifter width and thickness to be consistent with those of the optical wireless switch to ensure their seamless integration.

For the 1×3 optical wireless switch, the beam steering to address the upper or lower receiver requires a phase shift $\alpha = \pm 120°$. To achieve a phase shift of $+120°$ (or $-120°$), the phase shifter requires an energy of 2.63 pJ. In the present work, since we are considering that each OPA is constructed by $N_{ant} = 3$ identical taper antennas, therefore, we need three electro-optic phase shifters for beam steering. As an example, to address the upper receiver a phase shift $\alpha = +120°$ is required at the transmitting OPA. To achieve the required phase shift between the adjacent antennas in the OPA, input phases $[-120°, 0°, +120°]$ must be applied at the lower, central and upper antenna of the transmitting OPA. The overall energy required by the three phase shifters to achieve the beam steering is, therefore, 5.26 pJ (2.63 pJ+0 pJ+2.63 pJ=5.26 pJ). As mentioned earlier, the beam of the receiving OPA should also be virtually steered in the direction of radiation maximum to maximize the received power. This can be achieved by applying a phase shift $-\alpha$ (i.e, $[+120°, 0°, -120°]$) between the antenna elements of the receiving OPA. Therefore, to direct the addressed receiver towards the transmitter, another 5.26 pJ of energy is required to drive the phase shifters at the receiving OPA. Thus, the total energy required to drive phase shifters to establish a steered connection is 10.52 pJ. As was shown in Fig. 4a–c, owing to its broadband operation over the entire C-band, the optical switch can allow transmission of different wavelength channels according to the WDM schemes. All the allocated WDM channels can be switched at the same time, thus making the power requirement for signal routing independent from the number of WDM channels.

Conclusion

We numerically investigated the OPA-based optical switch implemented in hybrid SiN-TFLN material platform. We demonstrated that this hybrid approach results in an improved performance as compared to SiN-only configuration, as the field is vertically confined mostly in the LN layer, and consequently the multipath propagation effects become less critical. The beam steering to address the different in-plane receivers can be achieved by properly adjusting the phase shift between the antenna elements of the OPAs. We also presented the design of SiN-TFLN electro-optic phase shifters needed to drive the required phase shift. It was demonstrated that phase shifter exhibits a $V_\pi L_\pi = 4.74$ V cm and requires a 5.93 pJ of energy to achieve a π phase shift. Moreover, our simulation results predicted that the total energy required by the 1×3 optical switch to direct data from the central receiver to the side receivers is 10.52 pJ. Our findings suggest that the hybrid SiN-TFLN approach can facilitate realization of high-performance optical wireless switches by avoiding direct etching of lithium niobate, and by mitigating the impact of multipath propagation effects in the multilayer structures. These LN-based wireless switches can be assembled together to form reconfigurable switching matrices in on-chip communication networks. This work opens new avenues for on-chip wireless switching technology, offering a promising solution to overcome drawbacks of wired connections. These wireless switches offer power efficiency, fast speed and broadband behavior, making them an attractive choice for next-generation photonic interconnects in photonic computing, biosensing applications, wireless communication systems and data centers.

Data availability

The data that support the findings of this study are available from the corresponding author upon reasonable request.

Received: 18 August 2025; Accepted: 6 October 2025
Published online: 12 November 2025

References

1. Zhang, M., Wang, C., Kharel, P., Zhu, D. & Lončar, M. Integrated lithium niobate electro-optic modulators: When performance meets scalability. *Optica* **8**, 652–667. https://doi.org/10.1364/OPTICA.415762 (2021).
2. Luo, R., He, Y., Liang, H., Li, M. & Lin, Q. Highly tunable efficient second-harmonic generation in a lithium niobate nanophotonic waveguide. *Optica* **5**, 1006–1011. https://doi.org/10.1364/OPTICA.5.001006 (2018).
3. Krasnokutska, I., Tambasco, J.-L.J., Li, X. & Peruzzo, A. Ultra-low loss photonic circuits in lithium niobate on insulator. *Opt. Exp.* **26**, 897–904. https://doi.org/10.1364/OE.26.000897 (2018).
4. Wang, C., Zhang, M., Stern, B., Lipson, M. & Lončar, M. Nanophotonic lithium niobate electro-optic modulators. *Opt. Exp.* **26**, 1547–1555. https://doi.org/10.1364/OE.26.001547 (2018).
5. Li, Y. et al. High-performance Mach-Zehnder modulator based on thin-film lithium niobate with low voltage-length product. *ACS Omega* **8**, 9644–9651. https://doi.org/10.1021/acsomega.3c00310 (2023).
6. Wang, Z. et al. Fast-speed and low-power-consumption optical phased array based on lithium niobate waveguides. *Nanophotonics* **13**, 2429–2436. https://doi.org/10.1515/nanoph-2024-0066 (2024).
7. You, B. et al. Lithium niobate on insulator—Fundamental opto-electronic properties and photonic device prospects. *Nanophotonics* **13**, 3037–3057. https://doi.org/10.1515/nanoph-2024-0132 (2024).
8. Weigel, P. O. et al. Bonded thin film lithium niobate modulator on a silicon photonics platform exceeding 100 GHz 3-dB electrical modulation bandwidth. *Opt. Exp.* **26**, 23728–23739. https://doi.org/10.1364/OE.26.023728 (2018).
9. Valdez, F. et al. 110 GHz, 110 mw hybrid silicon-lithium niobate Mach-Zehnder modulator. *Sci. Rep.* **12**, 18611. https://doi.org/10.1038/s41598-022-23403-6 (2022).
10. Krishna, R. et al. Hybrid 3C-silicon carbide-lithium niobate integrated photonic platform. *Opt. Exp.* **32**, 14555–14564. https://doi.org/10.1364/OE.517840 (2024).
11. Ahmed, A. N. R. et al. Subvolt electro-optical modulator on thin-film lithium niobate and silicon nitride hybrid platform. *Opt. Lett.* **45**, 1112–1115. https://doi.org/10.1364/OL.381892 (2020).
12. Jiang, Y. et al. Monolithic photonic integrated circuit based on silicon nitride and lithium niobate on insulator hybrid platform. *Adv. Photon. Res.* **3**, 2200121. https://doi.org/10.1002/adpr.202200121 (2022).
13. Lee, W.-B., Kwon, Y.-J., Kim, D.-H., Sunwoo, Y.-H. & Lee, S.-S. Hybrid integrated thin-film lithium niobate-silicon nitride electro-optical phased array incorporating silicon nitride grating antenna for two-dimensional beam steering. *Opt. Exp.* **32**, 9171–9183. https://doi.org/10.1364/OE.518961 (2024).
14. Rabiei, P., Ma, J., Khan, S., Chiles, J. & Fathpour, S. Heterogeneous lithium niobate photonics on silicon substrates. *Opt. Exp.* **21**, 25573–25581. https://doi.org/10.1364/OE.21.025573 (2013).
15. Rao, A. et al. Heterogeneous microring and Mach-Zehnder modulators based on lithium niobate and chalcogenide glasses on silicon. *Opt. Exp.* **23**, 22746–22752. https://doi.org/10.1364/OE.23.022746 (2015).
16. Churaev, M. et al. A heterogeneously integrated lithium niobate-on-silicon nitride photonic platform. *Nat. Commun.* **14**, 3499. https://doi.org/10.1038/s41467-023-39047-7 (2023).
17. Krishna, R., Peng, Z., Hosseinnia, A. H. & Adibi, A. High-quality silicon nitride CMOS photonic devices. *IEEE Photon. Technol. Lett.* **36**, 763–766. https://doi.org/10.1109/LPT.2024.3396622 (2024).
18. Liu, J. et al. High-yield, wafer-scale fabrication of ultralow-loss, dispersion-engineered silicon nitride photonic circuits. *Nat. Commun.* **12**, 2236. https://doi.org/10.1038/s41467-021-21973-z (2021).
19. Li, Z. et al. Hybrid silicon nitride/lithium niobate electro-optical modulator with wide optical bandwidth and high RF bandwidth based on ion-cut wafer-level bonding technology. *Laser Photon. Rev.* e00138. https://doi.org/10.1002/lpor.202500138 (2025).
20. Qixiang Cheng, Rumley, S., Bahadori, M. & Bergman, K. Photonic switching in high performance datacenters [invited]. *Opt. Exp.* **26**, 16022–16043. https://doi.org/10.1364/OE.26.016022 (2018).
21. Xue, X. & Calabretta, N. Nanosecond optical switching and control system for data center networks. *Nat. Commun.* **13**, 2257. https://doi.org/10.1038/s41467-022-29913-1 (2022).
22. Chen, X., Lin, J. & Wang, K. A review of silicon-based integrated optical switches. *Laser Photon. Rev.* **17**, 2200571. https://doi.org/10.1002/lpor.202200571 (2023).
23. Dong-Yue Guo, Liu, J.-M. & Zhang, D.-L. LNOI photonic wire switch based on phase transition material. *Opt. Laser Technol.* **150**, 107972. https://doi.org/10.1016/j.optlastec.2022.107972 (2022).
24. Yue, W., Cai, Y. & Yu, M. Review of 2 × 2 silicon photonic switches. *Photonics* **10**, 564. https://doi.org/10.3390/photonics10050564 (2023).

25. Calò, G. et al. Design of reconfigurable on-chip wireless interconnections through optical phased arrays. *Opt. Exp.* **29**, 31212–31228. https://doi.org/10.1364/OE.427633 (2021).
26. Calò, G. et al. 4 × 4 integrated switches based on on-chip wireless connection through optical phased arrays. *Photonics* **10**, 367. https://doi.org/10.3390/photonics10040367 (2023).
27. Thonnart, Y. et al. POPSTAR: A robust modular optical NoC architecture for chiplet-based 3D integrated systems. In *2020 Design, Automation & Test in Europe Conference & Exhibition (DATE)*. 1456–1461. https://doi.org/10.23919/DATE48585.2020.9116214 (2020).
28. Guo, Y. et al. Integrated optical phased arrays for beam forming and steering. *Appl. Sci.* **11**, 4017. https://doi.org/10.3390/app11094017 (2021).
29. Hsu, C.-P. et al. A review and perspective on optical phased array for automotive LiDAR. *IEEE J. Sel. Top. Quantum Electron.* **27**, 1–16. https://doi.org/10.1109/JSTQE.2020.3022948 (2021).
30. He, J., Dong, T. & Xu, Y. Review of photonic integrated optical phased arrays for space optical communication. *IEEE Access* **8**, 188284–188298. https://doi.org/10.1109/ACCESS.2020.3030627 (2020).
31. Abiri, B., Fatemi, R. & Hajimiri, A. A 1-D heterodyne lens-free optical phased array camera with reference phase shifting. *IEEE Photon. J.* **10**, 1–12. https://doi.org/10.1109/JPHOT.2018.2871823 (2018).
32. Notaros, J. Integrated optical phased arrays: Lidar, AR displays, biophotonics, and beyond. In *Photonics North (PN), Montreal, QC, Canada*. Vol. 1–2. https://doi.org/10.1109/PN58661.2023.10222994 (2023).
33. Calò, G. et al. Reconfigurable optical wireless switches for on-chip interconnection. *IEEE J. Quantum Electron.* **59**, 1–10. https://doi.org/10.1109/JQE.2022.3224778 (2023).
34. Khalid, M. et al. LNOI wireless switches based on optical phased arrays for on-chip communication. *IEEE J. Sel. Areas Commun.* **42**, 2054–2065. https://doi.org/10.1109/JSAC.2024.3399207 (2024).
35. Sabouri, S., Mendoza, L. A. & Jamshidi, K. Three-wavelengths integrated sin optical phased array for LiDAR and FSO data link applications. *Opt. Exp.* **32**, 44776–44798. https://doi.org/10.1364/OE.538606 (2024).
36. Lumerical Solutions. https://www.ansys.com/products/optics.
37. Yousefi, P., Khalid, M., Petruzzelli, V. & Calò, G. Design of thin-film lithium niobate power splitters and combiners based on multimode interference. *Opt. Quantum Electron.* **57**, 198. https://doi.org/10.1007/s11082-025-08060-z (2025).
38. Peng, Z. et al. Photonic crystal microring resonators on a hybrid silicon nitride-on-lithium niobate platform. *Opt. Lett.* **50**, 4886–4889. https://doi.org/10.1364/OL.565076 (2025).
39. Nanni, J. et al. Multi-path propagation in on-chip optical wireless links. *IEEE Photon. Technol. Lett.* **32**, 1101–1104. https://doi.org/10.1109/LPT.2020.3012877 (2020).
40. Alam, B. et al. Numerical and experimental analysis of on-chip optical wireless links in presence of obstacles. *IEEE Photon. J.* **13**, 1–11. https://doi.org/10.1109/JPHOT.2020.3046379 (2021).
41. Chen, G. et al. Advances in lithium niobate photonics: development status and perspectives. *Adv. Photon.* **4**, 034003. https://doi.org/10.1117/1.AP.4.3.034003 (2022).

Author contributions

M.K. set up the numerical model, performed the simulations and wrote the manuscript; M.S. contributed to numerical simulations; S.F. and G.B. performed code verification and analysed the numerical data and results; G.C. and V.P. conceived the study, reviewed, edited and supervised the project. All authors reviewed the manuscript.

Funding

This work was supported in part by the European Union – Next Generation EU under the Italian National Recovery and Resilience Plan (NRRP), Mission 4, Component 2, Investment 1.3, CUP D93C22000910001, partnership on "Telecommunications of the Future" (PE00000001 - program "RESTART"); and was partially supported by the European Union - Next Generation EU under the Italian National Recovery and Resilience Plan (NRRP), Mission 4, Component 2, Investment 1.3, CUP B53C22003970001, partnership on "Telecommunications of the Future" (PE00000001 - program "RESTART") - Project ODEONS.

Declarations

Competing interests

The authors declare no competing interests.

Additional information

Correspondence and requests for materials should be addressed to M.K.

Reprints and permissions information is available at www.nature.com/reprints.

Publisher's note Springer Nature remains neutral with regard to jurisdictional claims in published maps and institutional affiliations.